J. Fluid Mech. (2009), *vol.* 622, *pp.* 103–113. © 2009 Cambridge University Press
doi:10.1017/S0022112008005272 Printed in the United Kingdom

On the equilibration of a symmetrically unstable front via a secondary shear instability

JOHN R. TAYLOR AND RAFFAELE FERRARI†

Department of Earth, Atmospheric, and Planetary Sciences,
Massachusetts Institute of Technology, Cambridge, MA, USA

(Received 1 July 2008 and in revised form 6 November 2008)

The equilibration of a symmetrically unstable density front is examined using linear stability theory and nonlinear numerical simulations. The initial state, chosen to approximate conditions in the surface ocean, consists of a weakly stratified mixed layer above a strongly stratified thermocline. Each layer has a uniform horizontal density gradient and a velocity field in thermal wind balance. The potential vorticity (PV) in the mixed layer is negative, indicating conditions favourable for symmetric instability. Once the instability reaches finite amplitude, a secondary Kelvin–Helmholtz (K-H) instability forms. Linear theory accurately predicts the time and the wavenumber at which the secondary instability occurs. Following the secondary instability, small-scale turbulence injects positive PV into the mixed layer from the thermocline and from the upper boundary, resulting in a rapid equilibration of the flow as the PV is brought back to zero. While the physical parameters used in this study correspond to typical conditions near a surface ocean front, many of the conclusions apply to symmetric instabilities in the atmosphere.

1. Introduction

The stability of an inviscid axisymmetric vortex was first studied by Rayleigh (1917) who showed that inertial instability can occur when the absolute value of the angular momentum decreases with radius. While the base state considered by Rayleigh consisted of a balance between the pressure gradient and the centrifugal force, inertial instability can also occur when the pressure gradient is in geostrophic balance with the Coriolis force. Consider a pressure gradient p_x in the x-direction. The corresponding geostrophic flow is given by $V_g = p_x/(f\rho_0)$. Note that ρ_0 is a reference density used in the Boussinesq approximation, which will be applied here in both the analysis and the numerical simulations. The Coriolis frequency f will be assumed to be constant, and Cartesian coordinates will be used for simplicity. Inertial instability of the geostrophic flow is possible when $f\partial\mathscr{M}/\partial x < 0$, where $\mathscr{M} = V_g + fx$ is the absolute momentum. Spatial variations in the fluid density ρ further modify the instability in the ocean and the atmosphere. In this case, so-called symmetric instability can occur when $f\partial\mathscr{M}/\partial x|_\rho < 0$, where the subscript ρ indicates that the derivative is evaluated along isopycnal surfaces (Holton 1992). When a uniform lateral density gradient in the x-direction is in 'thermal wind' balance with a velocity $V(z)$, so that $V_z = (-g/f\rho_0)\rho_x$, the criteria for inviscid symmetric instability can be written

† Corresponding author address: Department of Earth, Atmospheric and Planetary Sciences, 54-1420, 77 Massachusetts Ave. Cambridge, MA, 02139, USA. Email: rferrari@mit.edu

https://doi.org/10.1017/S0022112008005272 Published online by Cambridge University Press

(Stone 1966)

$$f(\nabla \mathscr{M} \times \nabla \rho) \cdot \hat{\boldsymbol{j}} < 0 \quad \rightarrow \quad M^4/f^2 - N^2 > 0, \tag{1.1}$$

where $M^2 = -(g/\rho_0)\rho_x$, $N^2 = -(g/\rho_0)\rho_z$ is the buoyancy frequency and $\hat{\boldsymbol{j}}$ is the unit vector in the y-direction. The criteria for instability can be cast in terms of the gradient Richardson number of the base flow, with instability possible if $Ri_0 = N^2/V_z^2 < 1$. Symmetric instability can develop at density fronts when the balanced horizontal density gradient is sufficiently large to overcome the stabilizing influences of the vertical stratification and rotation.

Alternatively, the criteria for symmetric instability can be expressed in terms of P_0, the Ertel's potential vorticity (PV), with instability arising when

$$f P_0 = \frac{-f}{\rho_0}(\nabla \times \boldsymbol{U}_g + f\hat{\boldsymbol{k}}) \cdot \nabla \rho < 0, \tag{1.2}$$

where $\boldsymbol{U}_g$ is the background geostrophic flow and $\hat{\boldsymbol{k}}$ is the vertical unit vector. As pointed out by Thorpe & Rotunno (1989) this presents a paradox: in the inviscid adiabatic limit for which the instability was first analysed, Ertel's theorem states that PV is materially conserved. Therefore, in an unbounded region with $f P_0 < 0$ everywhere, the unstable motions cannot make $f P_0 = 0$, as is necessary to equilibrate the inviscid instability. This paradox is overcome in real situations where the bulk PV of a given volume can be changed either through a boundary PV flux or by mixing with another volume of fluid with a different PV.

Thorpe & Rotunno (1989) examined a symmetrically unstable flow using two-dimensional numerical simulations. In one case, they considered an initial state with a uniform negative PV bounded from above and below by flat walls. When the boundary conditions allowed a flux of PV into the domain, they found that the volume-averaged PV increased primarily through a viscous flux at the boundaries. They also considered a situation with an isolated region of negative PV, surrounded by positive PV fluid. In this case, the symmetric instability broke the unstable region into smaller patches with alternating signs of PV. Eventually, the patches became small enough that the eddy viscosity and diffusivity used in the numerical model were sufficient to prevent symmetric instability within each patch. Hence, the entrainment of high-PV patches into the unstable region stabilized the low modes.

Throughout most of the ocean interior, the stratification is strong enough to prevent symmetric instability, i.e. $f P_0 > 0$ (O'Dwyer & Williams 1997). Two notable exceptions are the boundary layers at the top and bottom of the ocean (Allen & Newberger 1998; Haine & Marshall 1998), where turbulent mixing is strong enough to greatly reduce, if not eliminate, the stratification. Without the stabilizing influence of stratification, lateral density gradients can generate negative PV anomalies more readily, i.e. M^4/f^2 overcomes N^2 in (1.1). Recently, regions with negative PV have been observed at strong fronts in the surface mixed layer (Thomas & Lee 2005).

In the absence of sharp density fronts, inertial instability can also occur at low latitudes where f is small (see e.g. Hua, Moore & Gentil 1997; Dunkerton 1981; Griffiths 2003*a*,*b*). Griffiths (2003*b*) invoked a secondary Kelvin–Helmholtz (K-H) instability to explain why the scale associated with equatorial inertial instabilities was larger than predicted by linear theory. The numerical simulations of Griffiths (2003*b*) did not directly resolve the K-H billows but used a shear adjustment scheme to parameterize their effect. The parameterized momentum mixing acted like an effective viscosity on the large scales and increased the wavelength of the most unstable mode. One important constraint was the use of a vertically periodic domain with a constant

https://doi.org/10.1017/S0022112008005272 Published online by Cambridge University Press

background vertical stratification. With this assumption, vertical fluxes induced by the K-H instability were unable to change the bulk properties of the system. There was also a very large-scale separation between the size of the K-H-induced turbulence and the meridional extent of the unstable zone. Therefore, the equilibration mechanism proposed by Thorpe & Rotunno (1989) of entraining small patches of positive PV was not very effective. In the configuration considered by Griffiths (2003*b*), it appears that the K-H instability was not able to directly aid in the equilibration of the flow.

Despite the progress made by previous studies, questions remain as to how symmetrically unstable flows in the ocean and atmosphere equilibrate. The goal of this study is to examine the equilibration of a symmetrically unstable front with $fP_0 < 0$. We propose a new mechanism for this equilibration, namely enhanced vertical fluxes induced by the secondary K-H instability. In the ocean and atmosphere, the thermocline and the stratosphere represent ubiquitous reservoirs of high-PV fluid. The turbulence that is expected to develop from the K-H instabilities can be quite effective at mixing in the vertical direction and can rapidly equilibrate a symmetric instability by exchanging fluid with the high-PV reservoir.

2. Linear stability analysis

A linear stability analysis for a symmetrically unstable front can be used to estimate when secondary shear instabilities will develop. Consider a background density field $\overline{\rho} = -(\rho_0/g)(M^2x + N^2z)$ with a velocity $\boldsymbol{U}_g = V(z)\hat{\boldsymbol{j}}$ in thermal wind balance. For simplicity, the base velocity has no vertical relative vorticity. Small amplitude perturbations to the base flow, $\boldsymbol{u}'(x, z, t)$ and $\rho'(x, z, t)$, are assumed to be independent of the y (along-front) direction. The assumption of along-front homogeneity effectively excludes baroclinic instabilities from this system. Stone (1970) showed that when $0.25 < Ri_0 < 0.95$, the y-independent symmetric modes are the fastest-growing instabilities. By linearizing the governing equations with respect to the basic state, assuming that the perturbations are hydrostatic, and using a normal mode form in an infinite domain, i.e.

$$\boldsymbol{u}' = \boldsymbol{u}_0 \mathrm{e}^{\mathrm{i}kx + \mathrm{i}mz + \sigma t}, \tag{2.1}$$

the growth rate of the unstable symmetric modes is found to be (Stone 1966)

$$\sigma = \left(\frac{M^4}{N^2} - f^2 - N^2 \left(\frac{k}{m} - \frac{M^2}{N^2} \right)^2 \right)^{1/2} - \nu\left(k^2 + m^2\right). \tag{2.2}$$

Note that when $\nu = 0$, σ depends on k and m only through the perturbation slope k/m. In this case, the maximum growth rate is associated with $k/m = M^2/N^2$, i.e. the most rapidly growing perturbations are aligned with isopycnals. Friction tends to stabilize the shortest modes and acts to slightly reduce the slope of the most unstable mode. This can be shown by expanding σ in a Taylor series about the inviscid slope, $s = s_0 + \nu/(H^2|f|)s_1 + \cdots$, where $s_0 = M^2/N^2$ and $\nu/(H^2|f|)$ is the small parameter for the expansion (likely to be very small in real oceanographic and atmospheric applications where ν is the molecular viscosity). The slope of the most unstable mode for fixed m is given by

$$s_{max} \simeq \frac{M^2}{N^2} \left[1 - \frac{2|f|\nu m^2}{N^2} \left(\frac{1}{Ri_0} - 1 \right)^{1/2} + \cdots \right], \tag{2.3}$$

which is less than s_0 for unstable modes with $Ri_0 < 1$.

https://doi.org/10.1017/S0022112008005272 Published online by Cambridge University Press

At a density front with a non-vanishing vertical stratification, the isopycnals are inclined from the vertical. As the along-isopycnal velocity associated with symmetric instability grows in amplitude, so will the vertical shear associated with the slanting motions. We showed that at leading order in $\nu/(|f|H^2)$, the most unstable mode is associated with motions primarily along isopycnals and hence does not affect the density field, i.e. $\rho'_z \simeq 0$. The minimum gradient Richardson number associated with along-isopycnal velocity perturbations is

$$Ri_g \simeq \min\left(\frac{N^2}{u_z'^2 + (v_z' + V_z)^2}\right) \simeq \frac{N^2}{u_0^2 m^2 Ri_0^{-1} \mathrm{e}^{2\sigma t} + 2|V_z u_0 m|\left(Ri_0^{-1} - 1\right)^{1/2} \mathrm{e}^{\sigma t} + V_z^2}. \tag{2.4}$$

The Miles–Howard theorem states that K-H instability is possible when $Ri_g < 1/4$ somewhere in the flow. A linear mode with an initial amplitude u_0 and a vertical wavenumber m can therefore be expected to first become K-H unstable at a time

$$t_{KH} = \frac{1}{\sigma} \ln\left(\left|\frac{V_g}{u_0}\right|\right) + \frac{1}{\sigma} \ln\left(\frac{Ri_0}{mH}\left(\sqrt{3} - \sqrt{Ri_0^{-1} - 1}\right)\right), \tag{2.5}$$

where $V_g = V_z H$. Note that (2.5) applies only when $0.25 < Ri_0 < 1$ since when $Ri_0 < 0.25$ the initial state will be directly unstable to K-H, and for $Ri_0 > 1$ the flow will be stable to the primary symmetric instability. The first term on the right-hand side of (2.5) is the time at which the symmetric instability reaches finite amplitude, i.e. $|\boldsymbol{u}'| \simeq V_g$. Even for the smallest possible value of the vertical wavenumber, $m = 2\pi/H$, the second term on the right-hand side of (2.5) is negative in the relevant range $0.25 < Ri_0 < 1$. Therefore, the secondary K-H instability will always occur before the symmetric motions become fully nonlinear. For a given initial amplitude distribution $u_0(k, m)$, (2.5) can be minimized numerically to find the first mode to become K-H unstable. In the next section, we show that this result compares well with the onset of K-H instability in the nonlinear numerical simulations.

3. Numerical simulations

3.1. *Setup*

In order to test the hypothesis that the secondary K-H instabilities can stabilize a developing symmetric instability, we have conducted numerical simulations of a symmetrically unstable region bounded from above by a free-slip surface and bounded from below by a region with a large positive PV. A very fine mesh grid was used to explicitly resolve the K-H billows. Such a fine resolution would be prohibitive in a three-dimensional simulation and we therefore neglect variations in the along-front direction, as in several previous studies (e.g. Thorpe & Rotunno 1989; Griffiths 2003*b*). The parameters used for the simulations reflect conditions typical of a front in the oceanic mixed layer, although the conclusions also apply to dry symmetric instability in the atmosphere. (We will not consider the influence of moist processes that are likely important in the troposphere.)

The initial state consists of two layers, a weakly stratified surface mixed layer from $-50\ \mathrm{m} < z < 0$ and a strongly stratified thermocline from $-100\ \mathrm{m} < z < -50\ \mathrm{m}$, each with a uniform vertical density gradient. In order to mimic a lateral front, a constant background horizontal density gradient is used so that the isopycnal slope is $\gamma_{ML} = M^2/N_{ML}^2 = 0.047$ in the mixed layer and $\gamma_\infty = M^2/N_\infty^2 = 0.0047$ in the thermocline. Based on the initial vertical density gradient and the thermal wind shear, the initial gradient Richardson numbers for the upper and lower layers are

https://doi.org/10.1017/S0022112008005272 Published online by Cambridge University Press

$N^2_{ML} = 9 \times 10^{-6}\ \mathrm{s}^{-2}$	$N^2_{\infty} = 9 \times 10^{-5}\ \mathrm{s}^{-2}$	$M^2 = -4.2 \times 10^{-7}\ \mathrm{s}^{-2}$	$f = 10^{-4}\ \mathrm{s}^{-1}$
$P_{0,ML} = -9.2 \times 10^{-11}\ \mathrm{m}^{-1}\ \mathrm{s}^{-1}$	$P_{0,\infty} = 7.3 \times 10^{-10}\ \mathrm{m}^{-1}\ \mathrm{s}^{-1}$	$\nu = 10^{-4}\ \mathrm{m}^2\ \mathrm{s}^{-1}$	$\kappa = 10^{-4}\ \mathrm{m}^2\ \mathrm{s}^{-1}$

TABLE 1. Simulation parameters. Subscript ML denotes a property of the mixed layer, subscript ∞ denotes a property of the thermocline.

$Ri_{ML} = N^2_{ML} f^2 / M^4 = 0.5$ and $Ri_{\infty} = N^2_{\infty} f^2 / M^4 = 5$, so that the base flow is stable with respect to K-H instability everywhere, but is unstable to symmetric instability in the upper layer. Dimensional parameters used in the simulation are listed in table 1.

The initial velocity field consists of a thermal-wind balanced velocity $V(z)$ and a white noise with an amplitude of 10^{-4} m s^{-1} added to perturb the initial state. Before starting the simulations, the velocity field is projected onto a divergence free subspace. In order to simplify the boundary conditions, the density field is decomposed into a linear background gradient and a perturbation from that state: $\rho(x, z, t) = \rho_B(x) + \rho'(x, z, t)$. Periodic boundary conditions are applied in the x-direction to ρ' and $\boldsymbol{u}'$, while $\rho_B(x)$ and $V(z)$ are assumed to be constant in time. Although the background horizontal density gradient is kept fixed, the PV of the mixed layer is able to increase by developing correlations between vorticity and density gradients (see (1.2)). The use of periodic lateral boundary conditions allows us to avoid inflow/outflow conditions, which are very difficult to impose for turbulent flows such as those that are of interest here.

The domain sizes of $L_x = 1$ km and $L_z = 100$ m were chosen to be large enough to accommodate the most unstable symmetric mode. A uniform grid of $(N_x, N_z) = (1024, 128)$ points was used, which is sufficient to resolve the K-H billows. The top and bottom boundary conditions are no normal flow with the vertical gradients of the total density and velocity set to the initial state, i.e.

$$\left.\begin{array}{llll} u_z = 0, & v_z = M^2/f, & w = 0, & \rho_z = (-\rho_0/g)N^2_{\infty} \ @ \ \mathrm{z} = -\mathrm{H} \\ u_z = 0, & v_z = M^2/f, & w = 0, & \rho_z = (-\rho_0/g)N^2_{ML} \ @ \ \mathrm{z} = 0 \end{array}\right\}. \tag{3.1}$$

These boundary conditions were chosen to minimize the influence of boundary forcing on the flow at early times. Note, however, that since the density gradients at the upper and lower surfaces differ, both density and potential vorticity are fluxed into the domain.

The Boussinesq non-hydrostatic governing equations are solved using a CFD code described in detail in Taylor (2008). Derivatives in the horizontal direction are treated with a pseudo-spectral method while vertical derivatives are treated with second-order finite differences on a staggered grid. Time stepping is mixed implicit/explicit with viscous terms calculated using Crank–Nicolson and all other terms treated with a low-storage third-order Runge–Kutta method. In order to stabilize the numerical simulations, a constant viscosity of $\nu = 10^{-4}$ m^2 s^{-1} is used. Since the viscosity is two orders of magnitude larger than the molecular value, the simulations can be considered as either being at a low Reynolds number or using an eddy viscosity to represent unresolved turbulence. Taking the latter view, the Prandtl number is set to $Pr = 1$. This is consistent with unstratified turbulent scaling and is chosen since the unresolved scales in the simulations are less than 1 m where stratification should not play a dominant role.

https://doi.org/10.1017/S0022112008005272 Published online by Cambridge University Press

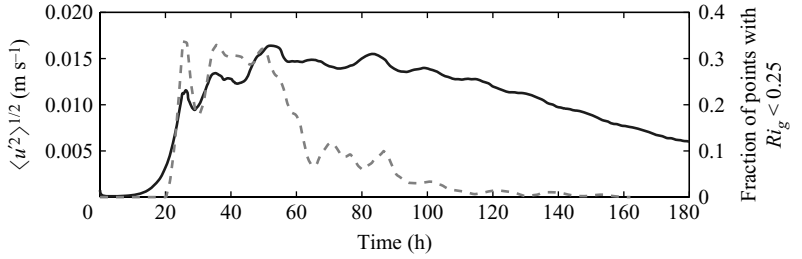


FIGURE 1. Temporal evolution of root mean square cross-front velocity (solid line) and the fraction of points with $Ri_g < 0.25$ (dashed curve), both averaged throughout the mixed layer, $-50 \text{ m} < z < 0$.

3.2. *Results*

Linear stability theory predicts an exponential growth of the symmetrically unstable modes. The root mean square of the cross-front velocity grows exponentially for $t \lesssim 24$ h (see figure 1), after which time, the amplitude of the symmetric instability has become sufficiently large to trigger secondary K-H instabilities. The dashed curve in figure 1 shows the fraction of gridpoints in the mixed layer where the local gradient Richardson number Ri_g is less than 1/4. In order to estimate the initial amplitude of the most unstable mode, the divergence-free initial velocity field was projected onto the mixed-layer isopycnal slope and the resulting field was averaged over the mixed layer. Using this estimated perturbation amplitude of $u_0 = 9.4 \times 10^{-6}$ m s^{-1} and minimizing (2.5) for a fixed disturbance slope with $k/m = M^2/N^2$, it can be predicted that K-H instability first occurs at $t \simeq 19.3$ h for the mode with horizontal and vertical wavenumbers $k_{KH} \simeq 0.013$ m^{-1} and $m_{KH} \simeq 0.27$ m^{-1}, in relatively good agreement with the simulation results. The resulting turbulence extracts energy from the symmetrically unstable modes and thereby limits their amplitude, as also found by Griffiths (2003*b*).

The transfer of energy from the unstable symmetric modes to smaller scales via the K-H instability can be seen in figure 2(*a*), where the spectral energy of the cross-front velocity is plotted as a function of time and the logarithm of the horizontal wavenumber. The cross-front velocity spectra are computed for each vertical level, and the spectral energy is then averaged across the mixed layer. For $t \lesssim 24$ h, the unstable modes grow exponentially, while viscosity damps the highest modes. In § 2 we showed that for $\nu/(|f|H^2) \ll 1$, unstable symmetric modes have $k/m \simeq M^2/N^2$. The cutoff horizontal wavenumber is then expected to be

$$k_c^2 = \frac{f}{\nu}\left(\frac{1}{Ri_0} - 1\right)^{1/2}\left(1 + \frac{N^4}{M^4}\right)^{-1} + H^{-2}O\left(\frac{\nu}{|f|H^2}\right). \tag{3.2}$$

For the parameters used in this simulation, $k_c \simeq 0.047$ m^{-1}. Once K-H instabilities fully develop at $t \simeq 24$ h, energy is transferred from the primary symmetric instability to higher wavenumbers. Note the formation of a secondary peak in energy for $k = 0.2 - 0.3$ m^{-1}, which corresponds to the width of the K-H billows. Since the aspect ratio of the billows is expected to be of the order of one, this is consistent with the prediction for m_{KH}, the vertical wavenumber of the first symmetric mode to become K-H unstable.

The onset of the secondary K-H instability coincides with a strong restratification and an increase in the mean fP_0 in the mixed layer. The evolution of the volume-averaged stratification and PV in the mixed layer is shown in figure 2(*b*).

https://doi.org/10.1017/S0022112008005272 Published online by Cambridge University Press

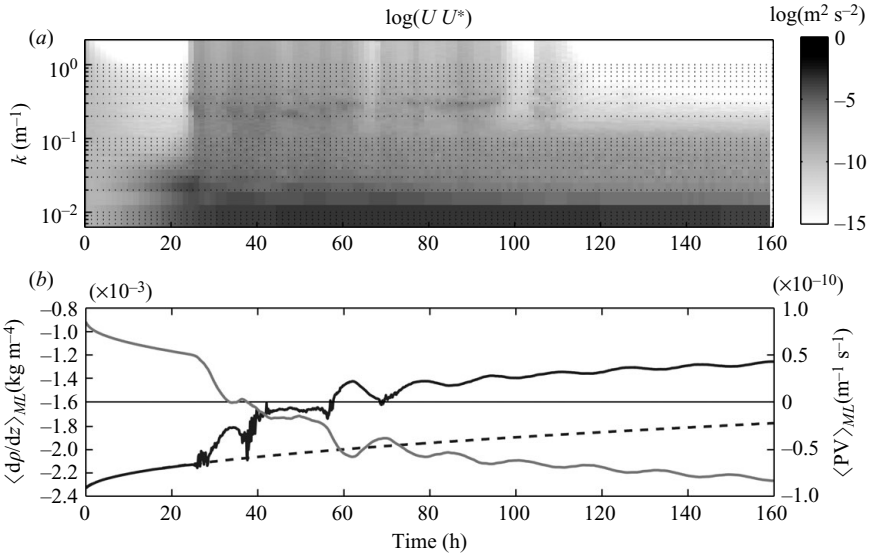


FIGURE 2. (*a*) Spectral energy of the streamwise velocity as a function of horizontal wavenumber and time, averaged over $-50 < z < 0$; (*b*) temporal evolution of Ertel's PV (grey) and the density gradient (black) averaged throughout the mixed layer. The dashed line shows the diffusive solution.

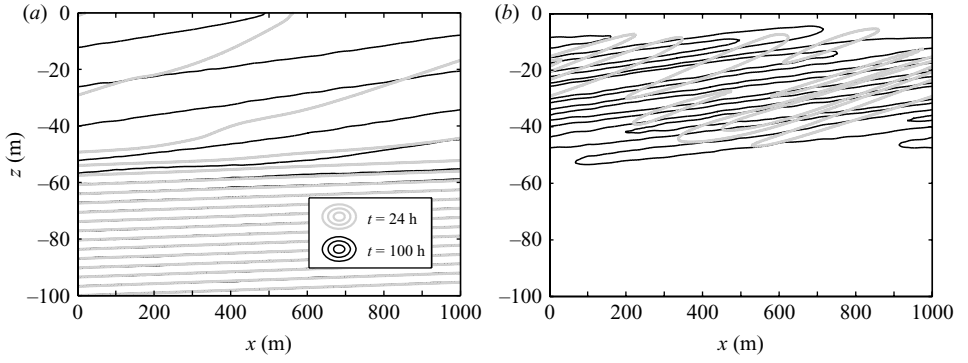


FIGURE 3. (*a*) Isopycnals and (*b*) velocity magnitude immediately preceding and following the period of active K-H instability, at $t = 24$ h (grey) and $t = 100$ h (black). The contour interval for isopycnals is 0.03 kg m^{-3} and that for velocity magnitude is 0.01 m s^{-1}.

Note that the choice use of a discontinuous initial density gradient at the base of the mixed layer and a constant eddy viscosity lead to a large diffusive PV flux at early times. To quantify this diffusive flux, we have also plotted the change the mixed-layer PV found by solving one-dimensional diffusion equations for momentum and density without advection. This demonstrates that nearly all of the PV increase prior to the onset of K-H is due to diffusion and not the symmetric instability.

After about 40 h, less than 20 h after the onset of K-H, the mixed-layer PV has nearly reached zero and the mean state is neutral with respect to symmetric instability. Subsequently, the flow remains symmetrically stable, and the shear that acted as a source of energy for the K-H instability gradually decays. The instantaneous isopycnals and velocity magnitude at $t = 24$ h and $t = 100$ h, preceding and following the period of active K-H instability, are shown in figure 3. At both times, the

https://doi.org/10.1017/S0022112008005272 Published online by Cambridge University Press

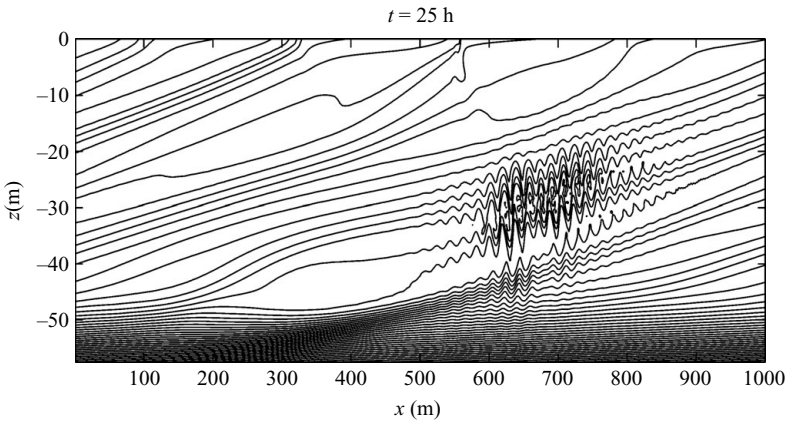


FIGURE 4. Isopycnals at a time just after the onset of the secondary K-H instability. Note that only a portion of the simulation domain is shown in order to focus on the small-scale features in the mixed layer.

streamlines are nearly parallel to the isopycnals, suggesting that these motions are associated with active or decaying symmetric instabilities.

Griffiths (2003*b*) found that a symmetric mode with scales much larger than the most unstable linear mode emerged after the onset of the secondary K-H instability. He argued that this mode was the most unstable when an effective turbulent viscosity due to the K-H motions was accounted for. We also observe the persistence of a large-scale mode following the period of active K-H instability, as seen in figures 2(*a*) and 3. In our simulations, the gravest mode grows in amplitude until $t \simeq 40$ h, i.e. when the PV becomes nearly zero and the symmetric instability is cured. This mode then gradually decays, but does so more slowly than the small-scale modes and appears to be a 'fossil' remnant of the symmetric instability. Although the fossil mode dominates the flow at late times, PV advection by this mode does not appear to play an important role in the equilibration of the symmetric instability, as surmised by Griffiths (2003*b*). The increase in mixed-layer PV appears to be associated instead with the K-H instabilities. When the flow is K-H unstable, the advective PV flux at the base of the mixed layer ($\langle P'w' \rangle$ at $z = -50$ m) is more than an order of magnitude larger than it is when $t > 100$ h and the flow is stable to K-H but a fossil mode is still present. The persistence of a fossil mode with a larger wavelength than the most unstable modes is consistent with atmospheric observations. The most unstable modes are probably difficult to observe, since the onset of the secondary K-H instability rapidly depletes their energy.

A visualization of the density field is shown in figure 4, at a time immediately following the onset of secondary K-H instability. The isopycnals in the mixed layer have become distorted by the symmetric instability, and a few regions of static instability are visible away from the region where K-H instability has developed. Although there are regions where the density gradient is very low, the region to first become K-H unstable is associated with a local shear maximum, but not a local minimum in the density gradient. Also, note the appearance of density fronts at the upper surface (figure 4). These surface fronts play an important role in fluxing positive PV into the mixed layer.

https://doi.org/10.1017/S0022112008005272 Published online by Cambridge University Press

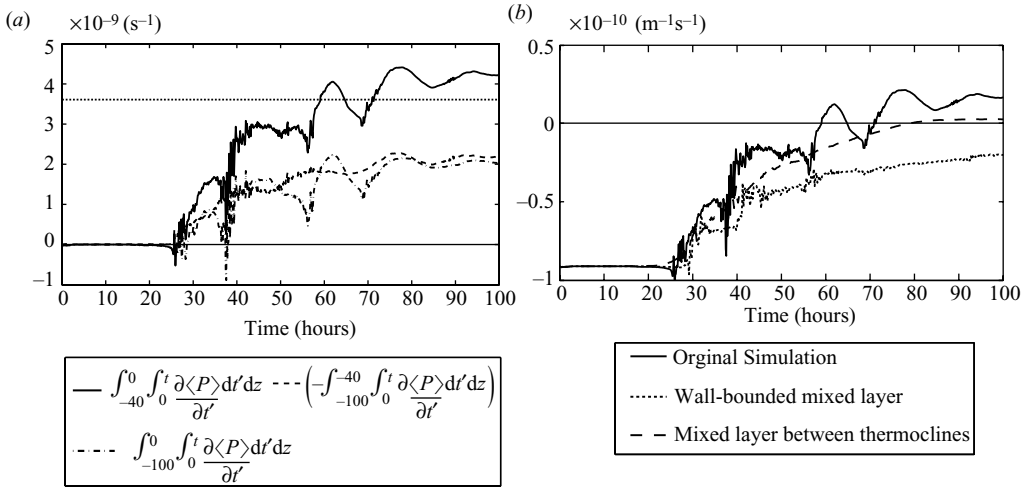


FIGURE 5. (*a*) Temporal change in the depth-integrated mixed-layer PV (solid line) with approximate fluxes from the thermocline (dashed line) and the upper surface (dash-dotted line). The increase in integrated PV needed to bring the entire mixed-layer PV to zero is indicated by a dotted line. (*b*) Volume-averaged mixed-layer PV for the three different simulations described in the legend. In order to remove the influence of the diffusive flux at the mixed layer/thermocline interface, the average excludes the 10 m bordering the thermoclines.

The evolution of the horizontally averaged PV can be written as

$$\frac{\partial \langle P \rangle}{\partial t} = -\frac{\partial}{\partial z}\left\langle Pw + \frac{1}{\rho_0}\kappa\nabla^2\rho((\nabla\times\boldsymbol{u})\cdot\hat{\boldsymbol{k}} + f) - \frac{1}{\rho_0}\nu\left(\nabla\rho\times\nabla^2\boldsymbol{u}\right)\cdot\hat{\boldsymbol{k}}\right\rangle, \tag{3.3}$$

where $<\cdot>$ denotes a horizontal average. Figure 5(*a*) shows the relative contributions of the PV flux to the interior of the mixed layer. Following the secondary K-H instability, the individual terms on the right-hand side of (3.3) vary over short time scales. Therefore, obtaining an accurate temporal integration of (3.3) is difficult. Instead, we rely on the observation that the flux of PV through the bottom of the domain ($z=-100$ m) is three orders of magnitude smaller than the PV flux inside the mixed layer. Therefore, the time-integrated PV flux at $z=-40$ m is, to within a very good approximation,

$$\langle J\rangle(z=-40\text{ m},t) \simeq -\int_0^t \int_{z=-100\,\mathrm{m}}^{z=-40\,\mathrm{m}} \left(\partial\langle P\rangle/\partial t'\right)\mathrm{d}z'\mathrm{d}t'. \tag{3.4}$$

This location ($z=-40$ m) was chosen to exclude the diffusive flux at the mixed layer/thermocline interface. Likewise, the time-integrated flux at the upper surface is approximately

$$\langle J\rangle(z=0,t) \simeq \int_0^t \int_{z=-100\,\mathrm{m}}^{z=0} \left(\partial\langle P\rangle/\partial t'\right)\mathrm{d}z'\mathrm{d}t'. \tag{3.5}$$

The PV flux at $z=-40$ m accounts for about half of the PV increase after the onset of the K-H instability, i.e. for $t>24$ h. The other half results from frictional and diffusive fluxes through the upper surface. While the surface boundary conditions fix the plane-averaged PV to the negative initial value, the PV *flux* at the surface is unconstrained. Based on a calculation of the individual terms in (3.3), the diabatic surface PV flux (the second term on the right-hand side of (3.3)) generally acts to

https://doi.org/10.1017/S0022112008005272 Published online by Cambridge University Press

decrease the mixed-layer PV. However, the diabatic term is more than compensated by a frictional flux of PV into the mixed layer (the final term on the right-hand side of (3.3)), leading to a net increase in PV owing to the surface fluxes.

To further illustrate the role of the boundary PV fluxes on the equilibration of the mixed-layer PV, two more simulations were conducted. The first simulation used rigid walls at the top and bottom of the mixed layer. Each wall had the same boundary conditions as used in the original simulation at $z = 0$. The second simulation started with high-PV thermoclines above and below the mixed layer. The horizontal and vertical density gradients in the mixed layer and the thermocline were the same as in the original simulation. The temporal evolution of the integrated rate of change of the mixed-layer PV for all three simulations is shown in figure 5(*b*). Note that in the simulation with a wall-bounded mixed layer, the PV at the centre of the mixed layer does return to zero, but since the PV near the walls remains at the initial negative value, the average is somewhat less than zero. Despite the difference in boundary conditions, the increase in mixed-layer PV is comparable in all three simulations. It therefore appears that the rate of PV injection into the mixed layer is largely set by the mixed-layer instabilities and not by the particular choice of boundary conditions (as long as a net PV flux is allowed).

4. Discussion

We have examined the evolution of a uniform density front in an ocean mixed layer with an initially homogeneous negative PV, with the goal of identifying a mechanism that equilibrates the unstable front. Symmetric instability develops at the front with motions nearly aligned with isopycnals, but this instability alone does not significantly alter the bulk PV in the mixed layer. Shortly after reaching finite amplitude, the slantwise motions associated with the symmetric instability become unstable to a secondary K-H shear instability. Turbulence induced by the K-H instability entrains high PV from the thermocline and induces a positive frictional PV flux at the upper boundary until the mixed-layer PV is brought to zero and the primary symmetric instability shuts down. These observations support the conclusion of Thorpe & Rotunno (1989) that regions of negative PV are neutralized through a combination of turbulent mixing and boundary fluxes. Here, we have identified the secondary K-H instability as a mechanism by which energy is transferred from the symmetric instability to small-scale turbulence.

Griffiths (2003*b*) identified a similar secondary K-H instability in numerical simulations of an equatorial inertial instability. However, owing to the choice of periodic vertical boundary conditions, the resulting turbulence was unable to alter the bulk PV through vertical fluxes. The inertial instability was equilibrated instead through lateral mixing with the regions of high PV north and south of the equatorial front; the equilibration process was quite slow, taking between 20 and 30 days (Griffiths 2003*b*). In light of the results of the present study, it is possible that with realistic boundary conditions at the ground and at the tropopause, equatorial inertial instability could be equilibrated more rapidly by vertical mixing induced by the secondary K-H instability.

The nonlinear development of symmetric instability is important to the dynamics of the ocean and atmosphere for several reasons. First, symmetric instabilities might play an important role in arresting frontogenesis at boundaries. It is well established that fronts can develop as a result of strain by geostrophic eddies in the ocean and atmospheric boundary layers. However, it remains an open question as to what

https://doi.org/10.1017/S0022112008005272 Published online by Cambridge University Press

arrests the formation of the frontal singularities. The PV at these fronts is typically low and it is plausible to expect that conditions for symmetric instability are often encountered. Our results suggest that the vertical mixing associated with secondary K-H instabilities could rapidly equilibrate such fronts since the time scale associated with the secondary K-H instability is much smaller than that associated with the mesoscale strain field. In addition, the enhanced vertical fluxes would have important consequences for the mixing of biological and chemical tracers between the mixed layer and the thermocline.

It has been speculated that atmospheric frontal rainbands are often associated with symmetric instability, although one puzzle is that conditions in these regions are most often neutral with respect to symmetric instability (Emanuel 1988). Enhanced vertical exchange caused by the secondary K-H instabilities could play a role in rapidly bringing a region with a negative PV back to a neutral state. We found that a large-scale 'fossil' mode remained long after the symmetric instability was equilibrated. The persistence of this mode may be analogous to the slantwise-convective motions that have been observed at near-neutral atmospheric fronts.

This research was supported by NSF grant OCE-0612143 (R. F.). We thank Leif Thomas and Kerry Emanuel for helpful discussions.

REFERENCES

Allen, J. S. & Newberger, P. A. 1998 On symmetric instabilities in oceanic bottom boundary layers. *J. Phys. Oceanogr.* **28** (6), 1131–1151.

Dunkerton, T. J. 1981 On the inertial stability of the equatorial middle atmosphere. *J. Atmos. Sci.* **38**, 2354–2364.

Emanuel, K. A. 1988 Observational evidence of slantwise convective adjustment. *Mon. Weather Rev.* **116**, 1805–1816.

Griffiths, S. D. 2003*a* The nonlinear evolution of zonally symmetric equatorial inertial instability. *J. Fluid Mech.* **474**, 245–273.

Griffiths, S. D. 2003*b* Nonlinear vertical scale selection in equatorial inertial instability. *J. Atmos. Sci.* **60**, 977–990.

Haine, T. W. N. & Marshall, J. 1998 Gravitational, symmetric, and baroclinic instability of the ocean mixed layer. *J. Phys. Oceanogr.* **28**, 634–658.

Holton, J. R. 1992 *An Introduction to Dynamic Meteorology*, 3rd ed. Academic Press.

Hua, B. L., Moore, D. W. & Le Gentil, S. equilibration of equatorial flows. *J. Fluid Mech.* **331**, 345–371.

O'Dwyer, J. & Williams, R. G. 1997 The climatological distribution of potential vorticity over the abyssal ocean. *J. Phys. Oceanogr.* **27**, 2488–2506.

Rayleigh, L. 1917 On the dynamics of revolving fluids. *Proc. R. Soc. Lond.* A **93**, 148–154.

Stone, P. H. 1966 On non-geostrophic baroclinic stability. *J. Atmos. Sci.* **23**, 390–400.

Stone, P. H. 1970 On non-geostrophic baroclinic stability. Part II. *J. Atmos. Sci.* **27**, 721–726.

Taylor, J. R. 2008 Numerical simulations of the stratified oceanic bottom boundary layer. PhD thesis, University of California.

Thomas, L. N. & Lee, C. M. 2005 Intensification of ocean fronts by down-front winds. *J. Phys. Oceanogr.* **35**, 1086–1102.

Thorpe, A. J. & Rotunno, R. 1989 Nonlinear aspects of symmetric instability. *J. Atmos. Sci.* **46** (9), 1285–1299.

https://doi.org/10.1017/S0022112008005272 Published online by Cambridge University Press